

Observing the onset of pressure-driven K-shell delocalization

<https://doi.org/10.1038/s41586-023-05996-8>

Received: 18 July 2022

Accepted: 22 March 2023

Published online: 24 May 2023

 Check for updates

T. Döppner¹✉, M. Bethkenhagen^{2,3}, D. Kraus^{2,4,5}, P. Neumayer⁶, D. A. Chapman⁷, B. Bachmann¹, R. A. Baggott⁸, M. P. Böhme^{5,9,10}, L. Divol¹, R. W. Falcone⁴, L. B. Fletcher¹¹, O. L. Landen¹, M. J. MacDonald¹, A. M. Saunders¹, M. Schörner², P. A. Sterne¹, J. Vorberger⁵, B. B. L. Witte^{2,11}, A. Yi¹², R. Redmer², S. H. Glenzer¹¹ & D. O. Gericke¹³

The gravitational pressure in many astrophysical objects exceeds one gigabar (one billion atmospheres)^{1–3}, creating extreme conditions where the distance between nuclei approaches the size of the K shell. This close proximity modifies these tightly bound states and, above a certain pressure, drives them into a delocalized state⁴. Both processes substantially affect the equation of state and radiation transport and, therefore, the structure and evolution of these objects. Still, our understanding of this transition is far from satisfactory and experimental data are sparse. Here we report on experiments that create and diagnose matter at pressures exceeding three gigabars at the National Ignition Facility⁵ where 184 laser beams imploded a beryllium shell. Bright X-ray flashes enable precision radiography and X-ray Thomson scattering that reveal both the macroscopic conditions and the microscopic states. The data show clear signs of quantum-degenerate electrons in states reaching 30 times compression, and a temperature of around two million kelvins. At the most extreme conditions, we observe strongly reduced elastic scattering, which mainly originates from K-shell electrons. We attribute this reduction to the onset of delocalization of the remaining K-shell electron. With this interpretation, the ion charge inferred from the scattering data agrees well with ab initio simulations, but it is significantly higher than widely used analytical models predict⁶.

The compression needed to modify the most tightly bound electrons can be estimated by comparing the mean distance between ions, expressed by the Wigner–Seitz radius a_i , with the extent of the bound wavefunction for hydrogen-like ions, given by the Bohr radius a_Z (ref. 4), that is

$$a_i = \left(\frac{3}{4\pi n_i} \right)^{1/3} \quad \text{and} \quad a_Z = \frac{\hbar^2}{Ze^2 m_e}. \quad (1)$$

Here, n_i is the ion density, \hbar is Planck's constant divided by 2π , e is the elementary charge, m_e is the electron mass and Z is the charge of the nuclear core. For low densities, we have $a_i \gg a_Z$ and the K shell is undisturbed by neighbouring ions. With increasing compression, the K shell is first modified when the wavefunctions of neighbouring ions start to overlap, and subsequently the electrons are driven into delocalized, conducting states. However, the exact conditions at which this transition occurs and the magnitude of K-shell modifications preceding it is still unknown. In the environments of planets and stars, this transition, referred to as pressure ionization, is also competing with thermally driven ionization. The latter clearly dominates for burning stars but both processes play an important role in giant planets as well as brown, red and white dwarfs^{1–3,7}.

Recently, pressure-induced ionization has been observed for dense fluid hydrogen^{8,9}. However, hydrogen transforms from a molecular-insulating phase to an atomic-metallic phase and the additional breaking of molecular bonds might trigger an ionization pathway that is different from other light elements¹⁰. In our experiment, we use beryllium (Be) to access partial ionization and investigate possible K-shell modifications in extreme conditions. At least three electrons were removed by sufficiently heating the sample during compression. Ions that are not fully ionized have one remaining electron in a hydrogen-like state with a nuclear charge of $Z = 4$. For isolated ions, this bound-electron wavefunction is analytically known. Thus, probing the K shell can reveal their modification due to neighbouring ions with high sensitivity.

In the laboratory, the highly compressed states needed can be reached only dynamically and their transient nature requires probing on a subnanosecond timescale. Here we use laser-produced X-rays for radiography and X-ray Thomson scattering (XRTS). These kiloelectron-volt X-rays are known to be able to penetrate compressed matter and carry information on the quantum states that the electrons occupy¹¹. Indeed, XRTS yields sufficient information to determine the thermodynamic state of the sample and also allows to investigate the atomic structure in these extreme environments.

¹Lawrence Livermore National Laboratory, Livermore, CA, USA. ²Institute of Physics, University of Rostock, Rostock, Germany. ³École Normale Supérieure de Lyon, LGLTPE, CNRS UMR 5276, Lyon, France. ⁴Department of Physics, University of California Berkeley, Berkeley, CA, USA. ⁵Helmholtz-Zentrum Dresden-Rossendorf, Dresden, Germany. ⁶GSI Helmholtz-Zentrum für Schwerionenforschung, Darmstadt, Germany. ⁷First Light Fusion Ltd, Yarnton, UK. ⁸The John Adams Institute for Accelerator Science, Imperial College London, London, UK. ⁹Center for Advanced Systems Understanding (CASUS), Görlitz, Germany. ¹⁰Technische Universität Dresden, Dresden, Germany. ¹¹SLAC National Accelerator Laboratory, Menlo Park, CA, USA. ¹²Los Alamos National Laboratory, Los Alamos, NM, USA. ¹³Centre for Fusion, Space and Astrophysics, Department of Physics, University of Warwick, Coventry, UK. ✉e-mail: doeppner1@llnl.gov

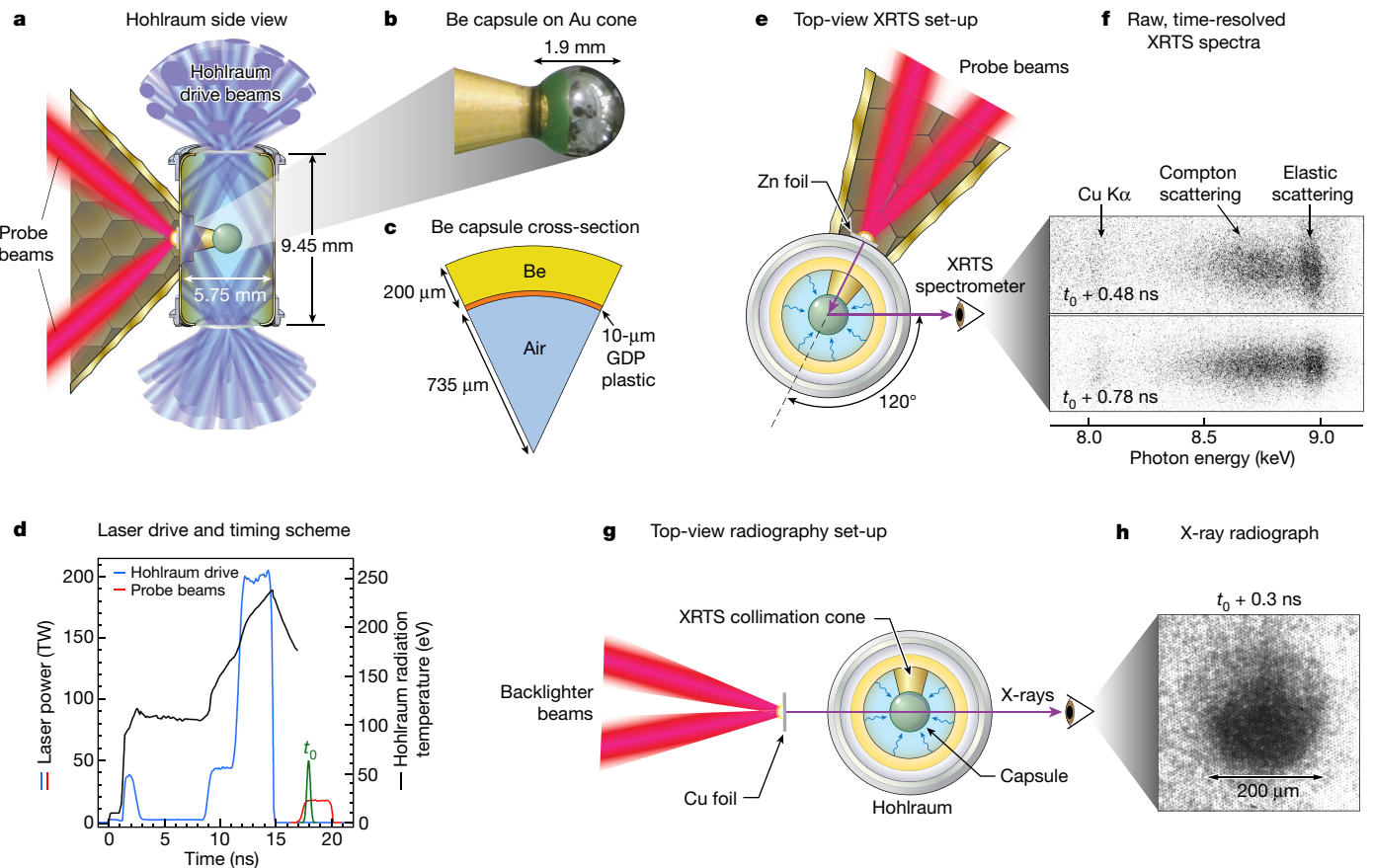


Fig. 1 | Schematic of the experiment and examples of raw data. **a,b**, Side view of the hohlraum target (**a**): 184 laser beams symmetrically implode a 1.9-mm-diameter beryllium capsule ($\rho = 1.82 \text{ g cm}^{-3}$) mounted on a gold cone (**b**) at the centre of the hohlraum. The X-ray source for probing is driven by eight laser beams, combined in groups of four beams each. **c**, Cross-section of the 200- μm -thick beryllium capsule. **d**, Evolution of the laser drive (blue) and resulting hohlraum radiation temperature (black). The probe beams (red) are timed shortly after the peak hotspot X-ray emission time, t_0 , when highest compression of the beryllium shell material is expected. **e**, Geometry of the XRTS experiment: eight laser beams heat a zinc foil, encapsulated by a gold shielding box to create 9-keV zinc $\text{K}\alpha$ emission for the XRTS measurement.

These X-rays are collimated by the inner gold cone. X-rays scattering off of the stagnating beryllium capsule are detected at 120° by the XRTS spectrometer¹⁴. **f**, Examples of raw XRTS spectra at two different probe times. The broader Compton peak at $t_0 + 0.78 \text{ ns}$ indicates increased compression. The shape of the inelastic Compton feature as well as its intensity ratio to the elastic Rayleigh feature are the input for our analysis. **g**, Geometry of the radiography experiment: eight laser beams heat a copper foil to create an area backscatterer of 8.3-keV photons. The shadow of the compressed capsule is observed through diamond windows in the hohlraum wall. **h**, Radiograph of the compressed beryllium shell demonstrating symmetric compression to approximately 200- μm diameter.

We employ laser-driven capsule implosions at the National Ignition Facility (NIF)⁵ to generate up to 30 times compressed beryllium. Figure 1 shows a schematic of the experiments and the temporal profile of the laser drive that delivers 0.8 MJ of 351-nm laser light into a cylindrical gold radiation cavity (hohlraum). The resulting thermal X-ray bath with a peak radiation temperature of 235 eV or 2.7 million kelvins (electronvolt (eV)) is used as unit of temperature throughout where $1 \text{ eV} = 11,604 \text{ K}$ ablates the outside of the 1.9-mm-diameter beryllium capsule, accelerating it inwards to peak velocities of 200 km s^{-1} . The shell stagnates about 18 ns after the start of the laser drive when most of the in-falling shell material is decelerated and compressed¹² (see Methods and Extended Data Fig. 4 for details of the target and implosion characteristics).

Eight additional laser beams are directed to heat a converter foil outside of the hohlraum (Fig. 1a) to create the X-rays for visualizing the capsule implosion dynamics through radiography or diagnosing the extreme states close to stagnation by XRTS. The latter is the primary diagnostics for our experiments (see refs. 11,13 and Methods). Scattered X-rays are collected through a diamond window in the hohlraum using a Bragg crystal spectrometer¹⁴ (Fig. 1e). Two independently timed XRTS spectra are recorded for each implosion, where each spectrum is integrated over 100 ps.

The experimental platform was used to field a series of four beryllium implosions: two characterizing the implosion dynamics during the stagnation phase using X-ray radiography and two experiments for XRTS measurements. All experiments were performed with the same target design and laser drive. NIF's outstanding laser-pulse-shaping capabilities enabled fielding all experiments with a high level of reproducibility. To compare probe times from different implosions, we measure the time of peak X-ray self-emission, t_0 , and reference all probe times with respect to this time¹².

Our XRTS measurements probe the beryllium shell conditions a few 100 ps after t_0 , when the majority of the remaining shell is assembled close to highest compression. In agreement with radiation hydrodynamic simulations¹², the radiography measurements show that the stagnating beryllium shell continues to accumulate material at the highest compression after t_0 (Fig. 1h for a transmission image at $t_0 + 300 \text{ ps}$), further increasing the volume with high-density beryllium. Based on the XRTS measurements, we observe the highest compression between 600 ps and 800 ps after t_0 .

The XRTS spectra are taken in back-scattering geometry (Fig. 1e) resulting in a momentum transfer of $k = 7.9 \text{ \AA}^{-1}$. This geometry has multiple advantages. First, most importantly, it yields a large Compton shift of 238 eV in the inelastic scattering feature, clearly separating it from

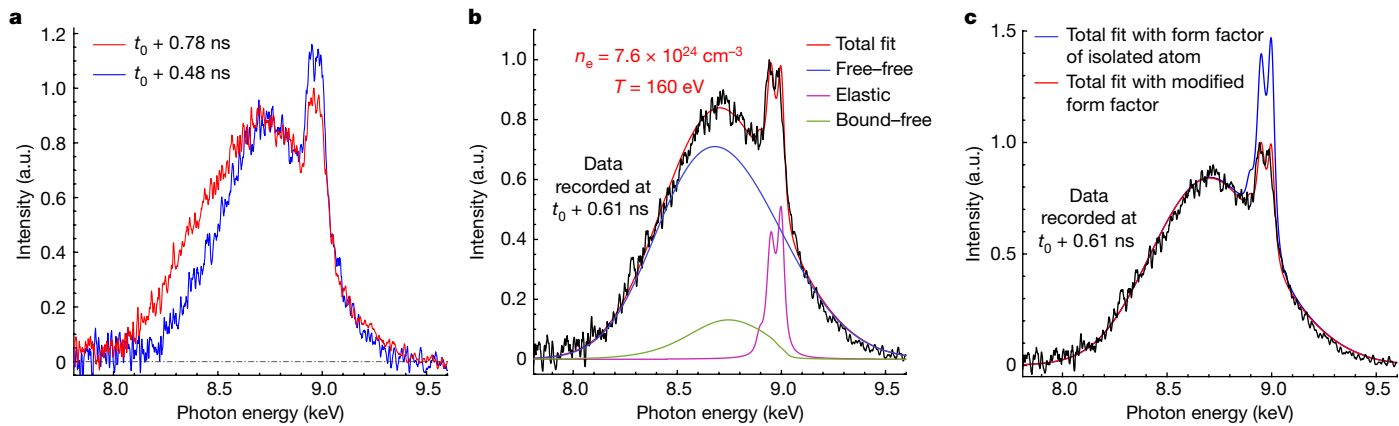


Fig. 2 | XRTS spectra and fits. **a**, XRTS spectra processed from raw data shown in Fig. 1f. The increase in width of the inelastic Compton peak at later time indicates higher compression, which is accompanied by a reduction in elastic scattering. **b**, Best fit and its three contributions to the XRTS spectrum recorded at $t_0 + 0.61$ ns using a temperature of $T = 160$ eV, a free electron density of $n_e = 7.6 \times 10^{24} \text{ cm}^{-3}$ and an ion charge of $\bar{Z} = 3.4$. Accordingly, the beryllium has been compressed to a mass density of $\rho = 34 \text{ g cm}^{-3}$ (see Table 1 for additional

details). **c**, Comparison of data (black) and the fit from **b** (red) with the standard model (for example, successfully applied in refs. 15,17–19) using hydrogen-like wavefunctions (blue). The best fit requires a K-shell wavefunction modification that reduces the ionic form factor f , and hence the Rayleigh weight W_R , by about 50% at the momentum transfer of $k = 7.9 \text{ \AA}^{-1}$ probed in the experiment. Spectra for the other probe times are provided in Extended Data Figs. 1–3.

the elastic Rayleigh peak. Second, it strongly mitigates uncertainties in the modelling as X-ray scattering with large momentum transfer dominantly samples individual electrons rather than complex collective excitations¹¹.

The back-scattering geometry also shows high sensitivity to the K-shell occupation and its wavefunction through the relative weight of the near-elastic Rayleigh feature, which can be expressed by¹¹

$$W_R(k) = [f(k) + q(k)]^2 S_{ii}(k), \quad (2)$$

where the ion-ion structure factor S_{ii} is close to unity and the screening contribution q is small for the large k value used here. Thus, the amplitude of the elastic scattering feature is determined by the ionic form factor f , which is the Fourier-transformed bound-electron density, that is, the square of the wavefunction of the remaining bound K-shell electron.

Figure 1f shows raw XRTS spectra for two implosion times. The elastic Rayleigh and inelastic Compton features are clearly visible and well separated. Taking into account spectral sensitivities of the scattering configuration, the spectra are processed (for details, see Methods) and shown in Fig. 2a, which allows for immediate conclusions: the spectrum at $t_0 + 0.78$ ns has a notably broader Compton feature, which is evidence for much higher electron density. The transition to a more parabolic shape, characteristic for scattering from electrons that show a Fermi distribution, also indicates states with quantum-degenerate free electrons¹¹. Higher compression is accompanied by substantially weaker elastic scattering, which per equation (2) indicates a reduction in the ionization degree, a reduction in the K-shell form factor, or a combination of both.

The scattering spectra can be modelled by three contributions^{11,15}: inelastic free-free and bound-free scattering as well as elastic scattering from bound and screening electrons (Methods). For the back-scattering geometry used here, fitting the inelastic component of the spectra yields a robust measurement of the plasma conditions, which previously has been demonstrated for solid-density and moderately compressed beryllium^{16–19}. Figure 2b shows an example of the fit obtained and quantifies its contributions. The largest one is due to inelastic scattering from free electrons. For the partially degenerate and partially ionized plasmas probed, the shape of this feature reveals both the free electron density and the temperature, which is particularly sensitive to the high-energy wing. In addition, contributions from bound-free scattering provide information on the ion charge state.

The plasma parameters obtained for the XRTS experiments are summarized in Table 1, showing that free electron densities above 10^{25} cm^{-3} and mass densities up to 55 g cm^{-3} have been created and probed. The primary quantities obtained are the electron density n_e and the temperature T . Much larger uncertainties arise for the charge state and, thus, the mass density and compression. The ratio of elastic to inelastic scattering strength can also be extracted directly from the data with high precision. A clear reduction of elastic scattering is observed for rows 3 and 4, which show the highest compression.

The elastic scattering strength is given by equation (2) and the ionic form factor f is here the critical quantity as there are relatively small uncertainties in the structure factor S_{ii} and the screening function q . The majority of XRTS measurements so far^{17–19} have been analysed applying the form factors for isolated ions. With this assumption, we either find that the amplitude of the elastic Rayleigh peak is strongly overestimated (Fig. 2c) or we have to assume a charge state of $\bar{Z} = 3.72$ for this case. This very high ionization would create inconsistencies in the fits and also in the description of the ionization balance⁴.

The observed reduced elastic scattering strength can be matched by modifying the wavefunction of the remaining K-shell electron, which has been predicted for plasmas close to the pressure-induced ionization threshold⁴. The high density of free electrons and the fields of nearby ions screen the ionic potential, leading to a less localized wavefunction that, however, remains almost unchanged close to the

Table 1 | Summary of plasma conditions extracted from the scattering spectra

Row	t (ns)	$n_e (10^{24} \text{ cm}^{-3})$	T (eV)	T_F/T	I_{el}/I_{inel}	\bar{Z}	ρ (g cm $^{-3}$)
1	0.31	1.34 ± 0.15	110_{-50}^{+15}	0.40	0.154 ± 0.008	3.0 ± 0.1	6.7 ± 1.0
2	0.48	1.9 ± 0.2	119_{-50}^{+15}	0.47	0.155 ± 0.008	3.05 ± 0.1	9.3 ± 1.3
3	0.61	7.6 ± 0.8	160 ± 20	0.88	0.087 ± 0.004	3.4 ± 0.1	34 ± 4
4	0.78	12 ± 1.5	160 ± 20	1.20	0.079 ± 0.004	3.3 ± 0.1	55 ± 8

The ratio of the Fermi temperature, calculated from the density of free (delocalized) electrons n_{el} and the plasma temperature, that is, T_F/T , indicates increasing quantum degeneracy with compression. The ratio of the elastic to the inelastic scattering strength, I_{el}/I_{inel} , is a direct observable and a strong constraint when inferring the average charge state, \bar{Z} , and hence mass density, ρ . The probe time t refers to the time after peak X-ray emission, t_0 (ref. 12). Rows 1 and 3 were recorded on experiment N170214-002-999, and rows 2 and 4 were recorded on experiment N160802-001-999. The errors are 1σ uncertainties.

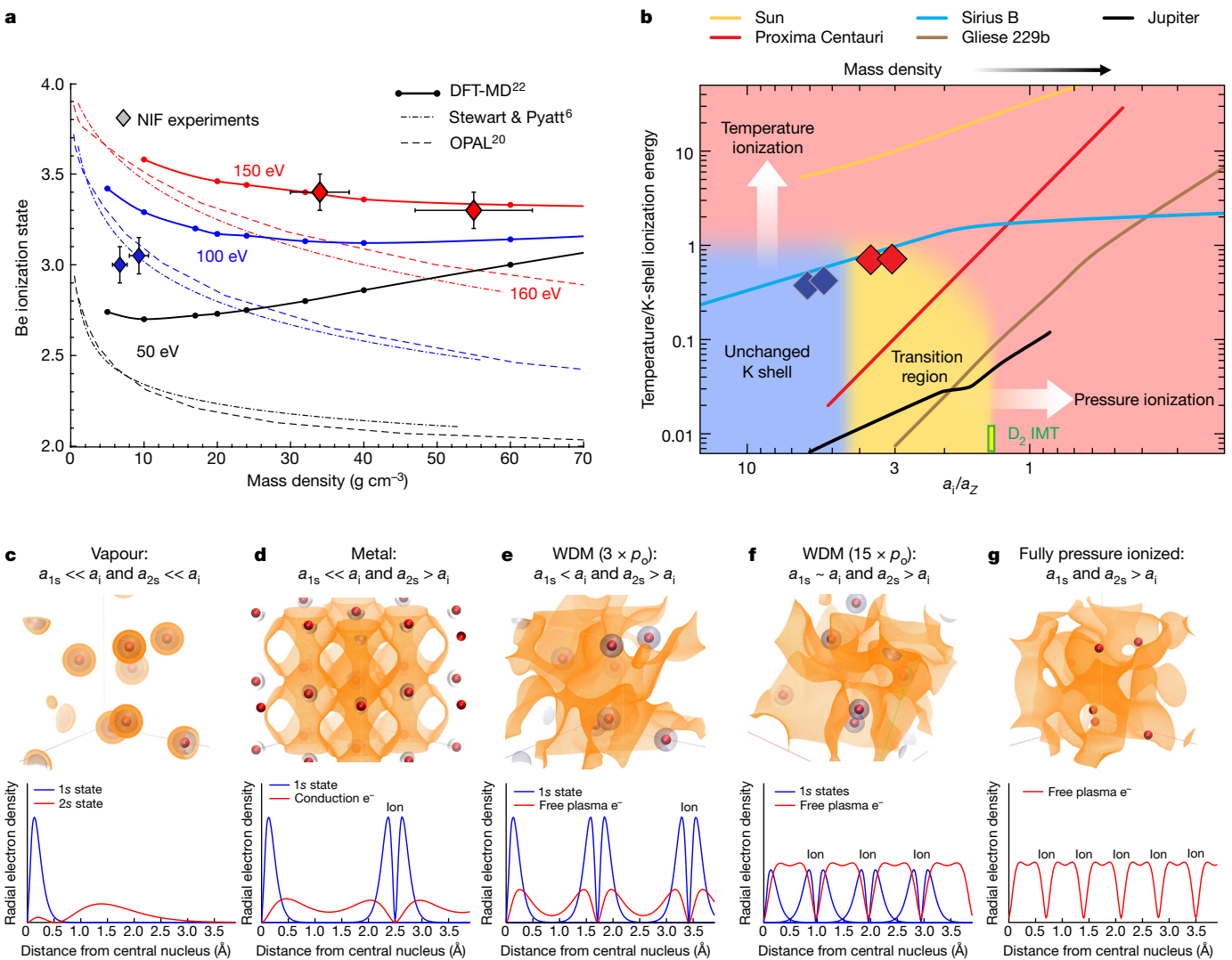


Fig. 3 | Summary of the experimental results. **a**, Comparison of the measured ionization degree with model prediction versus mass density. For mass densities higher than 30 g cm^{-3} , our experiments find significantly higher charge states than predicted by widely used ionization models^{6,20} but are in good agreement with quantum simulations (DFT-MD)²². The error bars indicate the fitting uncertainties. **b**, Relation of experimental observations (diamonds, colour-coded for temperature as in **a**) to plasma conditions in selected celestial bodies, ranging from giant planets (Jupiter⁷) to brown dwarfs (Gliese 229b⁷) to white dwarfs (Sirius B (D. Saumon, private communication)) to red dwarf stars (Proxima Centauri²⁸). To compare conditions for different elements in these objects, the thermal energy is normalized by the K-shell ionization energy and the compression, expressed in terms of the Wigner–Seitz radius, a_i , is normalized by the Bohr radius, a_z (equation (1)). We identify three regions with different K-shell properties: red, matter fully ionized by thermal effects, due to high compression or due to a combination of both; blue, matter with occupied

K shells unchanged from its atomic form at low temperatures and densities; yellow, the transition region tested by our experiments, where the K shells of neighbouring atoms start to overlap and, thus, being modified but matter is not yet fully ionized. At low temperatures, the density threshold for full pressure ionization is bound by experiments with shock-compressed deuterium that observed the insulator–metal transition (IMT) at $a_i/a_z = 1.37$ (ref. 8). **c–g**, Illustration of the electron configuration in beryllium at different compression compared to solid mass density ρ_0 : different isosurfaces of electron density (top) and radial electron density distribution around an ion for ideal systems (bottom). From left to right, the overlap of the wavefunctions increases with mass density, which first leads to the delocalization of the L shell and finally to K-shell ionization. See the main text for additional information. The conditions of row 3 in Table 1, shown in Fig. 2, correspond to the situation illustrated in **f**. WDM, warm dense matter.

nucleus. In Fourier space, this yields a reduction of the ionic form factor that becomes more prominent with increasing k and, thus, a considerably reduced Rayleigh peak at the wave number probed in our experiments.

Taking the simple form of Debye-like screening (Methods), we achieve a consistent description of the ionization state and the form of the K shell. Figure 2c shows that the large deviations between the data and modelling using the K shell of isolated ions can be reconciled when K-shell modifications due to screening are considered. As forward modelling of bound states in dense plasma environments is challenging, we circumvent this task here by treating the

screening length as a free parameter and employing the measured ratio of the elastic to inelastic scattering as an additional constraint. As the elastic Rayleigh peak is very sensitive to the ion charge state and localization of the remaining K-shell electron, we have established a consistent approach that yields the plasma conditions and tests our understanding of the density threshold for K-shell delocalization.

The directly measured ratio of elastic to inelastic scattering yields a well constrained ionization balance that is a crucial input for accurately modelling highly compressed matter. Figure 3a summarizes our results for the ion charge and compares it with predictions. The data

Article

points can be divided into two groups. For about five times compression (mass density $\rho \approx 10 \text{ g cm}^{-3}$; rows 1 and 2 in Table 1), the standard form factor of isolated ions yields self-consistent results. Hence, no K-shell modification is required despite a substantial reduction in binding energy⁶. However, the data for the highest compression show a reduction of the elastic scattering feature by 50% and 70% (rows 3 and 4 in Table 1, respectively). Thus, we find significant pressure-induced modifications to both the ionization balance and the form factor for these extreme conditions. Widely used ionization models^{6,20} predict significantly lower ionization than found experimentally. Moreover, they predict a decrease of the average ion charge state with density as three-body recombination increases more strongly with density than the impact of ionization potential depression²¹. In contrast, our experimental results are almost flat. Indeed, these exotic plasma conditions are extremely hard to model: here, the Coulomb interaction, the electron binding energy and the Fermi energy are all on a similar level, that is, on the order of 200 eV.

To cross-validate our analysis, we have performed ab initio density functional theory molecular dynamic (DFT-MD) simulations that incorporate the full quantum nature of the electrons and the strong forces between the ions (see Methods and ref. 22 for details). The results are in good agreement with the experiments for both the absolute value of the mean ionization state and the relatively flat trend at very high densities. The simulation data also show indications of the onset of delocalization for the strongly compressed cases: the K shell is dispersed into a broad band and a strong increase in the probability current between different bands is observed. This means a much higher probability of transferring electrons from one ion to another ion due to overlapping wavefunctions without increasing ionization. Thus, this behaviour is consistent with the onset of delocalization observed as a strong decrease of the elastic scattering strength in the experiments.

The bottom panels of Fig. 3 further illustrate the delocalization of electrons with increasing density and electron configurations of beryllium in different phases are shown. In the vapour phase (Fig. 3c), the atoms are well separated and both K-shell and L-shell electrons are localized around the nucleus. For the metal (Fig. 3d), localized L shells cannot exist as they are too large. Accordingly, the L shell is delocalized and transformed into conduction electrons whereas the deeply bound K shell is still intact. Previous experiments have heated and compressed beryllium into the warm dense-matter region^{16–19}. Except for thermal ionization, the electron configuration for isochorically heated beryllium and three times shock-compressed beryllium (Fig. 3e) does not change substantially when compared with the metal phase. Starting at about 15 times compression (Fig. 3f), the K-shell wavefunctions from neighbouring ions overlap, although they contain at most one bound electron due to temperatures beyond 100 eV. In this state, we find the onset of pressure-driven K-shell delocalization. Thus, a transition region between matter with unchanged K shells and a fully pressure-ionized state (Fig. 3g), predicted for even higher compression, is observed.

Figure 3b sets our experiments in relation to conditions found in astrophysical objects. To apply our findings for beryllium to objects with different compositions, we normalize the temperatures by the K-shell ionization energy. We also express the density by the Wigner–Seitz radius a_i , normalized by the extent of the K-shell wavefunction, that is, its Bohr radius a_z (equation (1)). Burning stars, such as our Sun, and smaller stars, such as the red dwarf Proxima Centauri, are fully thermally ionized. On the other hand, the deep interior of giant planets and white dwarfs are in the fully pressure-ionized state. Both regions are unaffected by our findings. However, the isentropes of dwarf stars and large planets pass through the transition region where the K shell is modified but not fully ionized. Indeed, our experiments scaled to oxygen matches a region in the outer layers of the white dwarf Sirius B well.

Most traditional models for the ionization balance predict an abrupt transition to the fully ionized state whereas our experiment shows

evidence for an extended transition region. Moreover, this region is bound by experimental data: its upper density can be established by the transition to a conducting phase observed in deuterium at $a_i/a_z = 1.37$ (refs. 8,9). The lower bound lies between our beryllium data with lower density at 9.3 g cm^{-3} ($a_i/a_z = 5.5$) and the high compression point at 34 g cm^{-3} ($a_i/a_z = 3.6$), which shows clear evidence for the K-shell modification through the strong reduction in elastic scattering.

In conclusion, we have uncovered strong modifications of the atomic physics in highly compressed light elements beyond temperature-driven ionization. In particular, our X-ray scattering data reveal, through the reduction of elastic scattering by more than 50%, that the K shell of beryllium is less deeply bound and the remaining bound electron is less localized at mass densities greater than 30 g cm^{-3} . This onset of delocalization is the precursor of pressure ionization and has been observed here experimentally. It reveals microscopic details of highly compressed matter and, thus, allows for unprecedented testing of theories and simulations. Comparisons with our experimental data show that widely used ionization models^{6,20} become increasingly inaccurate at extreme compression, raising questions about our ability to accurately model matter in the interior of planetary and stellar objects^{1–3} and in inertial confinement fusion experiments^{23–25}. Indeed, our finding of modified K shells can, through scaling, be applied to other low-Z elements such as carbon and oxygen, whose properties are crucial for the modelling of white dwarfs. Through the influence on radiation transport, both the ionization balance and the modified bound states may affect the cooling rate of white dwarfs and, ultimately, our estimate of the age of star populations^{26,27}.

Online content

Any methods, additional references, Nature Portfolio reporting summaries, source data, extended data, supplementary information, acknowledgements, peer review information; details of author contributions and competing interests; and statements of data and code availability are available at <https://doi.org/10.1038/s41586-023-05996-8>.

1. Burrows, A., Hubbard, W. B., Saumon, D. & Lunine, J. I. An expanded set of brown dwarf and very low mass star models. *Astrophys. J.* **406**, 158 (1993).
2. Chabrier, G. & Baraffe, I. Theory of low-mass stars and substellar objects. *Annu. Rev. Astron. Astrophys.* **38**, 337–377 (2000).
3. Kritcher, A. L. et al. A measurement of the equation of state of carbon envelopes of white dwarfs. *Nature* **584**, 51–54 (2020).
4. Kremp, D., Schlanges, M. & Kraeft, W.-D. *Quantum Statistics of Nonideal Plasmas* (Springer, 2005).
5. Moses, E. I., Boyd, R. N., Remington, B. A., Keane, C. J. & Al-Ayat, R. The National Ignition Facility: ushering in a new age for high energy density science. *Phys. Plasmas* **16**, 041006 (2009).
6. Stewart, J. C. & Pyatt, K. D. Lowering of ionization potentials in plasmas. *Astrophys. J.* **144**, 1203 (1966).
7. Becker, A., Bethkenhagen, M., Kellermann, C., Wicht, J. & Redmer, R. Material properties for the interiors of massive giant planets and brown dwarfs. *Astron. J.* **156**, 149 (2018).
8. Knudson, M. D. et al. Direct observation of an abrupt insulator-to-metal transition in dense liquid deuterium. *Science* **348**, 1455–1460 (2015).
9. Celliers, P. M. et al. Insulator–metal transition in dense fluid deuterium. *Science* **361**, 677–682 (2018).
10. Davis, P. et al. X-ray scattering measurements of dissociation-induced metallization of dynamically compressed deuterium. *Nat. Commun.* **7**, 11189 (2016).
11. Glenzer, S. H. & Redmer, R. X-ray Thomson scattering in high energy density plasmas. *Rev. Mod. Phys.* **81**, 1625 (2009).
12. Bishel, D. T. et al. Using time-resolved penumbral imaging to measure low hot spot X-ray emission signals from capsule implosions at the National Ignition Facility. *Rev. Scient. Instrum.* **89**, 10G111 (2018).
13. Kraus, D. et al. Platform for spectrally resolved X-ray scattering from imploding capsules at the National Ignition Facility. *J. Phys. Conf. Ser.* **717**, 012067 (2016).
14. Döppner, T. et al. Qualification of a high-efficiency, gated spectrometer for X-ray Thomson scattering on the National Ignition Facility. *Rev. Scient. Instrum.* **85**, 11D617 (2014).
15. Gregori, G., Glenzer, S. H., Rozmus, W., Lee, R. W. & Landen, O. L. Theoretical model of X-ray scattering as a dense matter probe. *Phys. Rev. E* **67**, 026412 (2003).
16. Glenzer, S. H. et al. Demonstration of spectrally resolved X-ray scattering in dense plasmas. *Phys. Rev. Lett.* **90**, 175002 (2003).
17. Lee, H. J. et al. X-ray Thomson-scattering measurements of density and temperature in shock-compressed beryllium. *Phys. Rev. Lett.* **102**, 115001 (2009).
18. Kritcher, A. L. et al. In-flight measurements of capsule shell adiabats in laser-driven implosions. *Phys. Rev. Lett.* **107**, 015002 (2011).

19. Fortmann, C. et al. Measurement of the adiabatic index in Be compressed by counterpropagating shocks. *Phys. Rev. Lett.* **108**, 175006 (2012).
20. Rogers, F. J., Swenson, F. J. & Iglesias, C. A. OPAL equation-of-state tables for astrophysical applications. *Astrophys. J.* **456**, 902 (1996).
21. Salzmann, D. *Atomic Physics in Hot Plasmas* (Oxford Univ. Press, 1998).
22. Bethkenhagen, M. et al. Carbon ionization at gigabar pressures: an ab initio perspective on astrophysical high-density plasmas. *Phys. Rev. Res.* **2**, 023260 (2020).
23. Hurricane, O. A. et al. Fuel gain exceeding unity in an inertially confined fusion implosion. *Nature* **506**, 343–348 (2014).
24. Zylstra, A. B. et al. Burning plasma achieved in inertial fusion. *Nature* **601**, 542–548 (2022).
25. Wurzel, S. E. & Hsu, S. C. Progress toward fusion energy breakeven and gain as measured against the Lawson criterion. *Phys. Plasmas* **29**, 062103 (2022).
26. Winget, D. E. et al. An independent method for determining the age of the Universe. *Astrophys. J.* **315**, L77 (1987).
27. Fontaine, G., Brassard, P. & Bergeron, P. The potential of white dwarf cosmochronology. *Publ. Astron. Soc. Pac.* **113**, 409 (2001).
28. Lütgert, B. J. et al. Platform for probing radiation transport properties of hydrogen at conditions found in the deep interiors of red dwarfs. *Phys. Plasmas* **29**, 083301 (2022).

Publisher's note Springer Nature remains neutral with regard to jurisdictional claims in published maps and institutional affiliations.

Springer Nature or its licensor (e.g. a society or other partner) holds exclusive rights to this article under a publishing agreement with the author(s) or other rightsholder(s); author self-archiving of the accepted manuscript version of this article is solely governed by the terms of such publishing agreement and applicable law.

© The Author(s), under exclusive licence to Springer Nature Limited 2023

Article

Methods

Capsule implosion set-up

The indirect-drive implosions of beryllium capsules are fielded at room temperature using gold hohlraums of 5.75-mm diameter, which are filled with neopentane (C_5H_{12}) at a density of 1.37 mg cm^{-3} . As shown in Fig. 1a, 184 of NIF's 192 beams are used to drive the hohlraum. These beams deliver a total of 0.8 MJ of laser light at 351 nm, heating the hohlraum to a peak radiation temperature of 235 eV. Implosion symmetry is achieved by fine-tuning the wavelength difference between the outer and the inner beams through cross beam energy transfer²⁹. The temporal hohlraum drive profile shown in Fig. 1d creates three shocks and is derived from symmetry-tuning experiments for laser fusion implosions^{23,30} but are reduced in peak laser power and duration and hence in implosion velocity. The latter is important to reduce the X-ray background for the scattering measurements near stagnation. Extended Data Fig. 4 illustrates the implosion characteristics and shows the plasma conditions of the imploding beryllium shell predicted by radiation hydrodynamic simulations.

Beryllium capsules were made by coating a 200-μm-thick beryllium shell ($\rho = 1.82 \text{ g cm}^{-3}$) onto a 10-μm-thick, spherical plastic layer (Fig. 1c) made out of glow discharge polymer (GDP; $\rho = 1.04 \text{ g cm}^{-3}$). As mid- and high-Z impurities increase elastic scattering of the sample, and hence complicate the interpretation of the XRTS measurement³¹, the beryllium capsules do not contain the copper-doped preheat shielding layer used in inertial confinement fusion implosion experiments³⁰. In addition, several measures were taken to minimize the accumulation of oxygen and other impurities that are introduced during the beryllium coating: (1) the nominal argon-assisted coating procedure was not used to avoid the implantation of argon ions into the beryllium shell; (2) the capsule was kept completely closed, that is, neither a cut-out was made to fit it onto the gold cone, nor a fill-tube hole was drilled; (3) accordingly, the high-temperature process to melt and remove the inner plastic layer was not applied. As a result, the capsule held air at ambient pressure at the time of the experiment. Pre-shot X-ray fluorescence spectroscopy showed that the dominant remaining impurity is oxygen at $0.75 \pm 0.25 \text{ at\%}$. At this impurity level, oxygen has negligible impact on the interpretation of the elastic scattering signal in the recorded XRTS spectra³¹. Additional impurities are below 0.1% and can be neglected for the analysis of the elastic scattering strength.

XRTS platform

The experimental platform for XRTS from indirectly driven imploding capsules at NIF is described in detail in refs. 13,32. In brief, eight beams of the NIF laser are used to heat a zinc foil located outside of the hohlraum wall to generate line emission at 9.0 keV from helium-like zinc ions (Fig. 1a). Large gold shields are placed around the zinc He α X-ray source to block the direct line of sight to the spectrometer. The probe X-rays are collimated by a $0.5 \times 1.0 \text{ mm}^2$ vertical slot located 3.0 mm from the sample and a re-entrant gold cone, which has an inner diameter of 550 μm at a distance of 1.0 mm from the centre of the hohlraum, and then scatter off the imploding beryllium capsule (see Fig. 1e for a schematic). Scattered X-rays are collected through a $0.8 \times 0.8 \text{ mm}^2$ diamond window and analysed with a Bragg crystal spectrometer using cylindrically curved highly oriented pyrolytic graphite coatings for high collection efficiency¹⁴. Two such crystals placed side by side direct their spectra to separate strips of a four-strip multi-channel plate (MCP) detector³³. These XRTS measurements are made more than 3.5 ns after the end of the main laser drive, when the hohlraum has cooled enough to not produce additional X-ray background in the XRTS spectra.

The raw XRTS data (Fig. 1f) are processed as follows. First, the signal is averaged over a 2.7-mm-wide region in the non-dispersive direction. The dispersion is determined from the spectrometer geometry¹⁴ and fine-tuned based on the location of the elastic scattering signal (zinc He α lines at 8.950 keV and 8.999 keV) and the Cu K α fluorescence

line (8.048 keV). Copper is present as an impurity below 0.01 at% in the beryllium and is photo-pumped by the zinc He α X-ray probe. A constant background is subtracted to zero out the spectrum at photon energies above 9 keV. In the next step, the spectra are corrected for transmissions through diagnostic filters, the hohlraum window and the material of the stagnated capsule, as well as for the spectral sensitivity of the highly oriented pyrolytic graphite crystal and the MCP detector. In addition, the nonlinear sampling of the spectrometer in energy space is taken into account. In the final step, we subtract the Cu K α line and a continuum with a temperature of $670 \pm 120 \text{ eV}$ (average over four datasets) such that the resulting spectrum converges to zero at the lower photon energies around 8 keV. The inferred continuum temperature is consistent with the hotspot temperature found in ref. 12 from differentially filtered hotspot imaging.

Radiography platform

The radiography measurements use the same geometry of the inner gold cone as the XRTS targets, but with the cone axis azimuthally rotated to place it perpendicular to the radiography line of sight (Fig. 1g). For the data shown in Fig. 1h, we utilized a copper He α area backscatterer emitting at 8.3 keV that is pumped by 8 beams of the NIF laser. Multiple time-resolved transmission images are recorded with a pinhole imager at sixfold magnification and 25-μm spatial resolution using a pinhole grid mapped onto a gated, four-strip MCP detector³⁴. To reference the timing of different implosions, we measure the time of peak X-ray emission, t_0 , using a large-pinhole, high-sensitivity imaging snout with a line of sight through the upper laser entrance hole¹². For the four experiments fielded with the implosion design and target configurations described in this paper, we find that t_0 varies by $\pm 35 \text{ ps}$ where most of the deviations can be explained by variations in delivered laser energy and beryllium shell mass. The two radiography experiments, N160801-001-999 and N170214-001-999 (Extended Data Fig. 5), show very good consistency for stagnation dynamics, implosion shape and t_0 , which demonstrates the excellent shot-to-shot reproducibility at the NIF.

Modelling of XRTS spectra

Our XRTS spectra are analysed with the widely used approach that has been successfully applied for analysing previous XRTS measurements (see, for example, refs. 31,35,36). In brief, the scattering cross-section is proportional to the total dynamic electron-electron structure factor $S(k, \omega)$ which, following the approach of Chihara^{11,37}, can be decomposed into three distinct contributions

$$S(k, \omega) = |f(k) + q(k)|^2 S_{ii}(k, \omega) + \bar{Z} S_{ee}(k, \omega) + (Z - \bar{Z}) \int S_{be}(k, \omega - \omega') S_s(k, \omega') d\omega'. \quad (3)$$

where $\hbar\omega$ is the energy change of the scattered photon, S_{ii} is the ion-ion structure factor, S_{ee} is the free-free dynamic structure factor, and S_{be} is the form factor of bound electrons undergoing Raman-like transitions to the continuum, which is modulated by the self-motion of the ions, S_s . The first term of equation (3) describes the elastic scattering, the second term the inelastic scattering from free electrons and the third term the inelastic scattering due to bound-free transitions. The various inelastic scattering contributions have been discussed in detail previously^{11,15,38}.

Here we focus on the elastic scattering. As shown in equation (3), the elastic scattering strength, often referred to as the weight of the Rayleigh peak $W_R(k)$, can be calculated from the ionic form factor, $f(k)$, the electronic screening cloud contribution, $q(k)$, and the static ion-ion structure factor $S_{ii}(k)$. As the plasma under study contains two distinct ions species with very different scattering properties, $W_R(k)$ needs to be generalized as^{39,40}

$$W_R(k) = \sum_{a,b} \sqrt{x_a x_b} [f_a(k) + q_a(k)][f_b(k) + q_b(k)] S_{ab}(k) \quad (4)$$

where a and b run over the ion species present in the sample, that is, Be³⁺ and Be⁴⁺ ions in the case of our experiments. x_a is the number density fraction of ions of species a , $f_a(k)$ is the ionic form factor of this species and $q_a(k)$ is its screening contribution. The microscopic ion structure is included via the partial ion–ion structure factors S_{ab} .

The ion–ion structure factor, S_{ii} , is calculated by the hypernetted-chain approach^{38,41}. We have benchmarked the hypernetted-chain results against our DFT-MD calculations, and find only small deviations in S_{ii} . Hence, the impact on the inferred ionization state is minimal. The related uncertainty is captured as part of the error bars in Fig. 3a. To calculate the screening cloud contribution, $q(k)$, we have implemented finite wavelength screening⁴² and tested, including against DFT-MD, that $q(k)$ remains small compared with $f(k)$.

Several ab initio approaches have been suggested to calculate XRTS spectra but they are mainly following the decomposition of Chihara (equation (3)) using results of ab initio calculations as inputs^{43–45}. Such an approach would leave our results almost unchanged as we have tested the input of our XRTS modelling against DFT-MD. So far, to our knowledge, only ref. 46 has successfully implemented full ab initio calculations of XRTS spectra including the elastic scattering feature without applying the Chihara decomposition. However, the simulations are computationally extremely expensive, and currently not practical for iteratively inferring plasma conditions from scattering spectra.

Modified ionic form factors

The form factor needed to model the elastic scattering strength (equation (2)) is the radial Fourier transform of the electron density around an ion. For undisturbed K shells as they occur in atomic systems, metals and slightly compressed warm dense matter (Fig. 3c–e), the analytic solution for hydrogen-like orbits can be applied. The majority of previous XRTS experiments^{16–19} on warm dense beryllium were successfully analysed under this assumption. Here, f remains hydrogen-like, and only its amplitude is modified due to the ionization level of the sample.

Modifications to the form factor owing to high compression can be modelled in a similar way. However, the K-shell wavefunction, and thus its density and Fourier transform, need to be calculated from numerical solutions of the Schrödinger equation. In this way, any modified form of the nuclear field can be incorporated. Here, we use a Debye-like potential to account for the screening of the plasma electrons and the influence of neighbouring ions. Despite this being a simplification of the full many-body problem, this approach allows to obtain the wavefunctions and the binding energy self-consistently.

The screening length is used as a free parameter as there does not exist an established and tested method for the reduction of the binding energy for given plasma conditions. It is determined by a self-consistent approach applying the elastic scattering strength: (1) form factor and binding energy are calculated from the Schrödinger equation for a given screening length; (2) the effective binding is used in a Saha equation to calculate the ion charge state; (3) these quantities define the predicted elastic scattering strength via equation (2); (4) this prediction is finally compared with the measured spectrum and iterated until agreement is obtained. As a result, we have a self-consistent set of values for the form factor, the ionization balance, the other plasma parameters and measured data that is based on fundamental concepts, namely the Schrödinger equation for a given potential and Boltzmann statistics for the bound states underlying the Saha equations. Testing this procedure with an effective Coulomb potential that uses an effective ion charge as a free parameter showed that the inferred average ionization state, \bar{Z} , is robust against the specific form of the effective nuclear potential that the remaining K-shell electron experiences.

XRTS data analysis and uncertainties

Here we report results produced by single-condition fits, which provide mass-averaged quantities over the sampled plasma volume. As we

probe after peak X-ray emission, the main shock wave has rebounded and strongly compresses and heats the dense material still streaming inwards (Extended Data Fig. 4 and ref. 12). For the highest compression (rows 3 and 4 in Table 1), the outgoing shock wave has completely passed through the probe volume. Although gradients persist, the related spectra are dominated by scattering from beryllium at high compression. The error bars for n_e and T reported in Table 1 are 1σ uncertainties based on the statistical analysis of an individual spectrum. \bar{Z} is extracted from analysing the ratio of elastic to inelastic scattering, I_{el}/I_{inel} , which yields robust results. The mass density, ρ , is derived from the measured electron density, n_e , and $\bar{Z} \cdot I_{el}/I_{inel}$ can be extracted directly from the experimental spectrum with high accuracy, and varies only very weakly with respect to the plasma parameters. We have tested this for a wide range of (\bar{Z} , n_e , T) combinations that provide a good fit to the spectrum when the elastic scattering is excluded, that is, for which I_{el} is a free parameter. This procedure yielded the 1σ uncertainties for I_{el}/I_{inel} reported in Table 1.

We note that the two lower-density datasets (rows 1 and 2 in Table 1) are probably probing a combination of material ahead and behind the rebounding shock, which is accounted for by the increased temperature error bars reported in Table 1.

DFT-MD simulations

DFT-MD simulations were performed with the Vienna Ab initio Simulation Package^{47–49}. We considered 32 beryllium atoms in the simulation box at densities up to 60 g cm^{-3} for three different temperatures at 50 eV, 100 eV and 150 eV. All electrons were treated explicitly using the Coulomb potential with a cut-off energy of 10 keV. The DFT-MD simulations were typically run for at least 20,000 time steps with a time step size between 5 as (150 eV) and 50 as (50 eV). The ion temperature was controlled by a Nosé–Hoover thermostat⁵⁰, the Brillouin zone was sampled at the Baldereschi mean value point⁵¹ and we employed the exchange-correlation functional of Perdew, Burke and Ernzerhof⁵². Subsequently, we determined the dynamic electrical conductivity via the Kubo–Greenwood formalism^{53,54} as an average of typically 20 snapshots chosen randomly from the DFT-MD trajectory. In those calculations, we increased the number of used bands even further and switched the k -point sampling to the Monkhorst–Pack $2 \times 2 \times 2$ grid for densities higher than 10 g cm^{-3} . The ionization state was derived by extracting the conduction–conduction conductivity and applying the Thomas–Reiche–Kuhn sum rule²².

Data availability

The three additional scattering spectra not shown in Fig. 2b are included as Extended Data Figs. 1–3. Additional data are available upon request from the corresponding author. Source data are provided with this paper.

Code availability

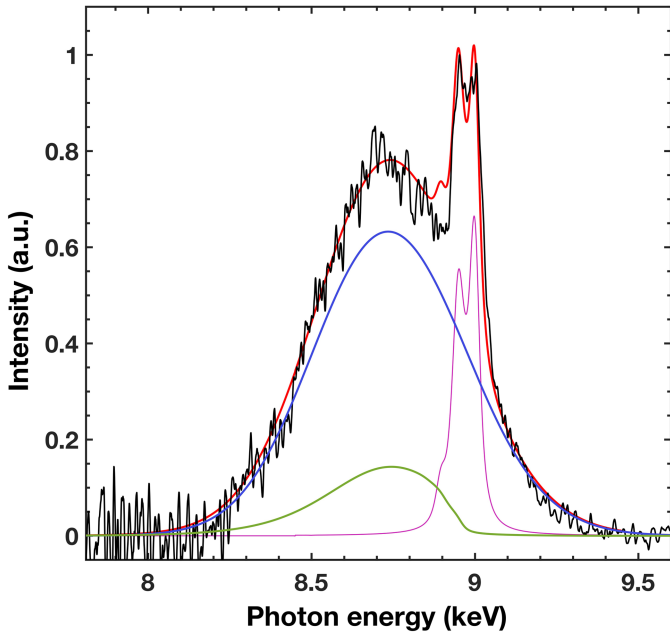
The Multi-Component Scattering Spectra (MCSS) code⁴⁰ for analysing X-ray Thomson scattering spectra is not publicly available. An open-source code is currently under development with support from some members of our team.

29. Michel, P. et al. Tuning the implosion symmetry of ICF targets via controlled crossed-beam energy transfer. *Phys. Rev. Lett.* **102**, 025004 (2009).
30. Kline, J. L. et al. First beryllium capsule implosions on the National Ignition Facility. *Phys. Plasmas* **23**, 056310 (2016).
31. Saunders, A. M. et al. Influence of argon impurities on the elastic scattering of X-rays from imploding beryllium capsules. *High Energy Dens. Phys.* **26**, 86–92 (2018).
32. Boehm, K.-J. et al. Design and engineering of a target for X-ray Thomson scattering measurements on matter at extreme densities and gigabar pressures. *Fusion Sci. Technol.* **70**, 324 (2016).
33. Döppner, T. et al. Improving a high-efficiency, gated spectrometer for X-ray Thomson scattering experiments at the National Ignition Facility. *Rev. Scient. Instrum.* **87**, 11E515 (2016).

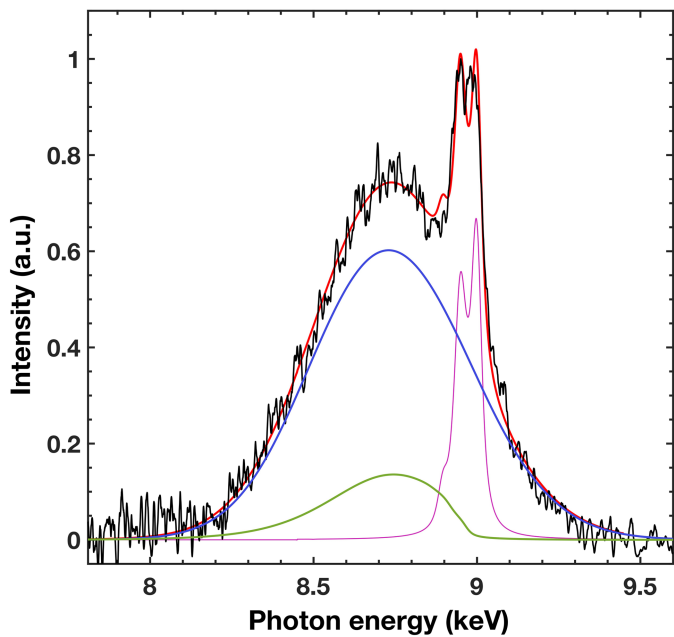
Article

34. Rygg, J. R. et al. 2D X-ray radiography of imploding capsules at the National Ignition Facility. *Phys. Rev. Lett.* **112**, 195001 (2014).
35. Fletcher, L. B. et al. Ultrabright X-ray laser scattering for dynamic warm dense matter physics. *Nat. Photon.* **9**, 274–279 (2015).
36. Kraus, D. et al. X-ray scattering measurements on imploding CH spheres at the National Ignition Facility. *Phys. Rev. E* **94**, 011202 (2016).
37. Chihara, J. Interaction of photons with plasmas and liquid metals-photoabsorption and scattering. *J. Phys. Condens. Matter* **12**, 231 (2000).
38. Chapman, D. A. *Probing the Dynamic Structure of Dense Matter Using X-ray Scattering*. PhD thesis, Univ. Warwick (2015).
39. Wünsch, K., Vorberger, J., Gregori, G. & Gericke, D. O. X-ray scattering as a probe for warm dense mixtures and high-pressure miscibility. *Europhys. Lett.* **94**, 25001 (2011).
40. Chapman, D. A. *User Guide and Theoretical Basis for the Multicomponent Scattering Spectra (MCSS) Thomson Scattering Analysis Code* (AWE, 2017).
41. Wünsch, K., Vorberger, J. & Gericke, D. O. Ion structure in warm dense matter: benchmarking solutions of hypernetted-chain equations by first-principle simulations. *Phys. Rev. E* **79**, 010201 (2009).
42. Chapman, D. A. et al. Observation of finite-wavelength screening in high-energy-density matter. *Nat. Commun.* **6**, 6839 (2015).
43. Plagemann, K.-U. Ab initio calculation of the ion feature in X-ray Thomson scattering. *Phys. Rev. E* **92**, 013103 (2015).
44. Vorberger, J. & Gericke, D. O. Ab initio approach to model X-ray diffraction in warm dense matter. *Phys. Rev. E* **91**, 033112 (2015).
45. Souza, A. N., Perkins, D. J., Starrett, C. E., Saumon, D. & Hansen, S. B. Predictions of X-ray scattering spectra for warm dense matter. *Phys. Rev. E* **89**, 023108 (2014).
46. Baczewski, A. D., Shulenburger, L., Desjarlais, M. P., Hansen, S. B. & Magyar, R. J. X-ray Thomson scattering in warm dense matter without the Chihara decomposition. *Phys. Rev. Lett.* **116**, 115004 (2016).
47. Kresse, G. & Hafner, J. Ab initio molecular dynamics for liquid metals. *Phys. Rev. B* **47**, 558–561 (1993).
48. Kresse, G. & Hafner, J. Ab initio molecular-dynamics simulation of the liquid-metal-amorphous-semiconductor transition in germanium. *Phys. Rev. B* **49**, 14251–14269 (1994).
49. Kresse, G. & Furthmüller, J. Efficient iterative schemes for ab initio total-energy calculations using a plane-wave basis set. *Phys. Rev. B* **54**, 11169–11186 (1996).
50. Nosé, S. A unified formulation of the constant temperature molecular dynamics methods. *J. Chem. Phys.* **81**, 511–519 (1984).
51. Baldereschi, A. Mean-value point in the Brillouin zone. *Phys. Rev. B* **7**, 5212–5215 (1973).
52. Perdew, J. P., Burke, K. & Ernzerhof, M. Generalized gradient approximation made simple. *Phys. Rev. Lett.* **77**, 3865–3868 (1996).
53. Kubo, R. Statistical-mechanical theory of irreversible processes. I. General theory and simple applications to magnetic and conduction problems. *J. Phys. Soc. Jpn* **12**, 570–586 (1957).
54. Greenwood, D. A. The Boltzmann equation in the theory of electrical conduction in metals. *Proc. Phys. Soc.* **71**, 585–596 (1958).
- formatting. The work of T.D., B.B., L.D., O.L.L., M.J.M., A.M.S. and P.A.S. was performed under the auspices of the US Department of Energy under contract no. DE-AC52-07NA27344, and was supported by Laboratory Directed Research and Development (LDRD) grant no. 18-ERD-033. The DFT-MD calculations were performed at the North-German Supercomputing Alliance (HLRN) facilities and at the IT and Media Center of the University of Rostock. M.B., M.S., B.B.L.W. and R.R. acknowledge support by the Deutsche Forschungsgemeinschaft (DFG) within the FOR 2440. M.B. was also partially supported by the European Horizon 2020 programme within the Marie Skłodowska-Curie actions (xICE grant number 894725). D.K. was supported by the Helmholtz Association under VH-NG-1141. D.K. and R.W.F. acknowledge support by the US Department of Energy, Office of Science, Office of Fusion Energy Sciences, award DE-AC02-05CH11231, and National Nuclear Security Administration, award DE-NA0003842. R.W.F. acknowledges support from the Department of Energy, National Nuclear Security Administration Award DE-NA0003842, and the Department of Energy, Office of Science, Office of Fusion Energy Sciences Awards DE-SC0021184 and DE-SC0018298. The work of L.B.F. and S.H.G. was supported by US Department of Energy, Fusion Energy Sciences under FEP 100182. The work of M.P.B. was partially supported by the Centre for Advanced Systems Understanding (CASUS), which is financed by Germany's Federal Ministry of Education and Research (BMBF) and by the Saxon state government out of the State budget approved by the Saxon State Parliament. We also acknowledge the NIF Discovery Science programme for providing access to the facility. This document was prepared as an account of work sponsored by an agency of the US government. Neither the US government nor Lawrence Livermore National Security, LLC, nor any of their employees makes any warranty, expressed or implied, or assumes any legal liability or responsibility for the accuracy, completeness, or usefulness of any information, apparatus, product, or process disclosed, or represents that its use would not infringe privately owned rights. Reference herein to any specific commercial product, process, or service by trade name, trademark, manufacturer, or otherwise does not necessarily constitute or imply its endorsement, recommendation, or favouring by the United States government or Lawrence Livermore National Security, LLC. The views and opinions of authors expressed herein do not necessarily state or reflect those of the US government or Lawrence Livermore National Security, LLC, and shall not be used for advertising or product endorsement purposes.
- Author contributions** P.N., R.W.F. and S.H.G. proposed the experiments and aided in obtaining experimental beam time at NIF. A.Y., L.D., T.D. and O.L.L. developed the Be implosion design. T.D. fielded the experiments together with D.K., B.B., M.J.M. and A.M.S. The XRTS spectra were analysed by T.D., M.P.B., D.K. and L.B.F. Additional data analysis and feedback on analysis methods were provided by P.N., O.L.L., B.B., M.J.M., M.S. and A.M.S. D.O.G., D.A.C., J.V., R.A.B., M.P.B. and P.A.S. provided results for the ionization in dense plasmas and developed the framework for modelling XRTS spectra. M.B., M.S., B.B.L.W. and R.R. performed and analysed the DFT-MD simulations. All co-authors provided input on the interpretation of the data and their impact on astrophysics and ICF. T.D. and D.O.G. wrote the paper.
- Competing interests** The authors declare no competing interests.
- Additional information**
Supplementary information The online version contains supplementary material available at <https://doi.org/10.1038/s41586-023-05996-8>.
Correspondence and requests for materials should be addressed to T. Döppner.
Peer review information *Nature* thanks Shinsuke Fujioka, Nigel Woolsey and the other, anonymous, reviewer(s) for their contribution to the peer review of this work. Peer reviewer reports are available.
Reprints and permissions information is available at <http://www.nature.com/reprints>.

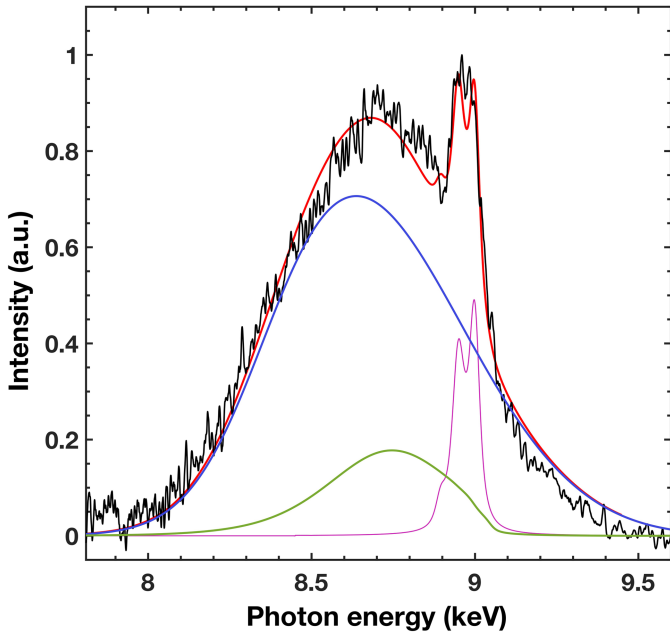
Acknowledgements We thank the entire NIF operations, diagnostics, target design and assembly teams for support; K. Boehm and P. di Nicola for coordinating the target builds; N. Rice and H. Huang for making and metrologizing the beryllium capsules; D. Kalantar and N. Masters for resolving any alignment and machine safety issues; B. Remington and J. Lütgent for reading the manuscript and providing feedback; and M. Meamber for helping with figure design and



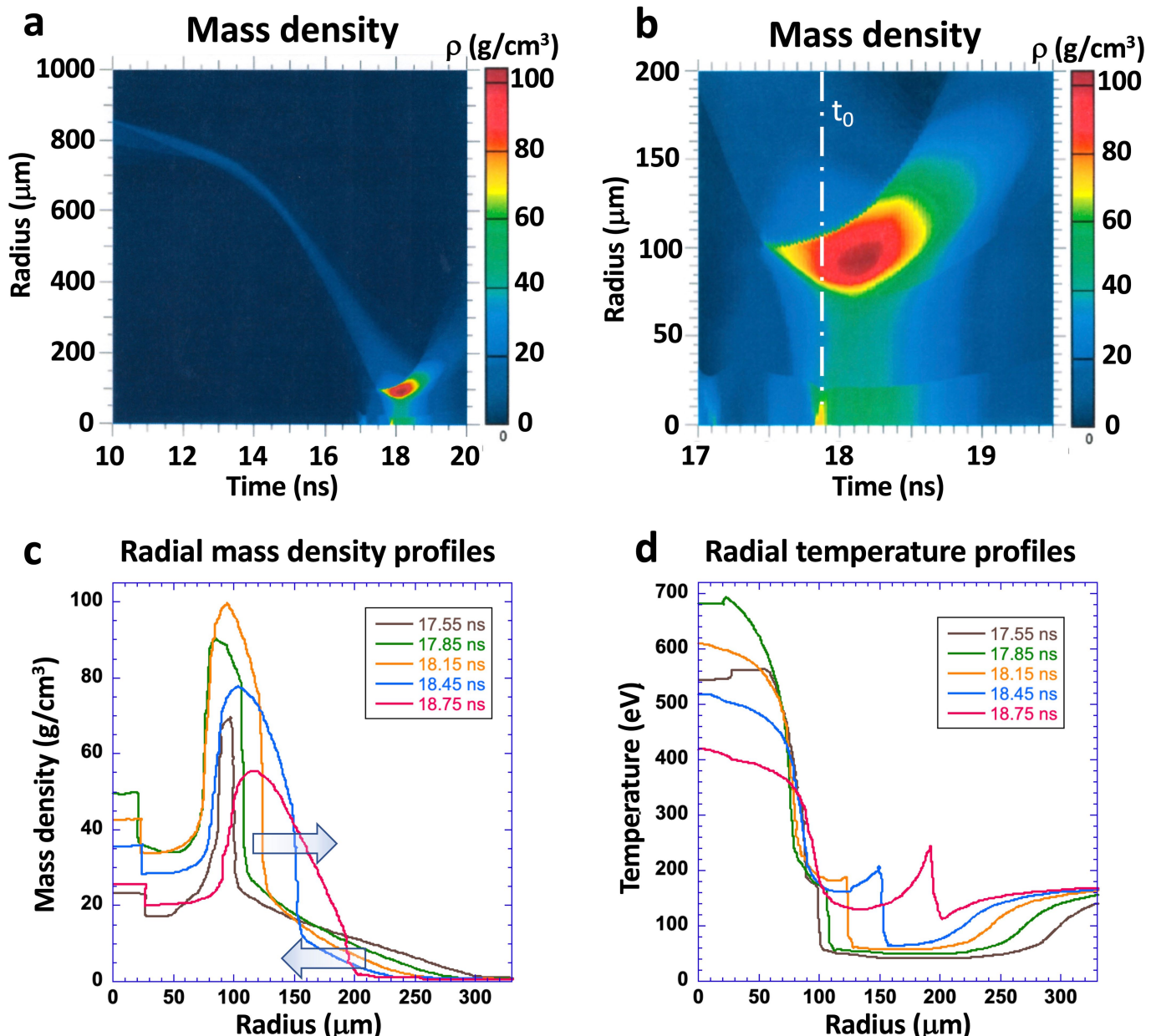
Extended Data Fig. 1 | X-ray Thomson scattering spectrum and fit for data set #1. The data (black) was recorded on experiment N170214-002-999 on the first spectrometer channel (strip 1) at 0.31 ns after peak emission, t_0 . The best fit (red), consisting of the free-free (blue), bound-free (green) and elastic (purple) scattering contributions, yields a temperature of $T = (110 \pm 15)$ eV, a free electron density of $n_e = (1.34 \pm 0.15) \times 10^{24}$ cm $^{-3}$ and an ion charge of $\bar{Z} = 3.0 \pm 0.1$ resulting in a mass density of $\rho = (6.7 \pm 1.0)$ g/cm 3 (see row #1 in Table 1).



Extended Data Fig. 2 | X-ray Thomson scattering spectrum and fit for data set #2. The data (black) was recorded on experiment N180602-001-999 on the first spectrometer channel (strip 1) at 0.48 ns after peak emission, t_0 . The best fit (red), consisting of the free-free (blue), bound-free (green) and elastic scattering (purple) contributions, yields a temperature of $T = (119 \pm 15)$ eV, a free electron density of $n_e = (1.9 \pm 0.2) \times 10^{24} \text{ cm}^{-3}$ and an ion charge of $\bar{Z} = 3.05 \pm 0.1$ resulting in a mass density of $\rho = (9.3 \pm 1.3) \text{ g/cm}^3$ (see row #2 in Table 1).

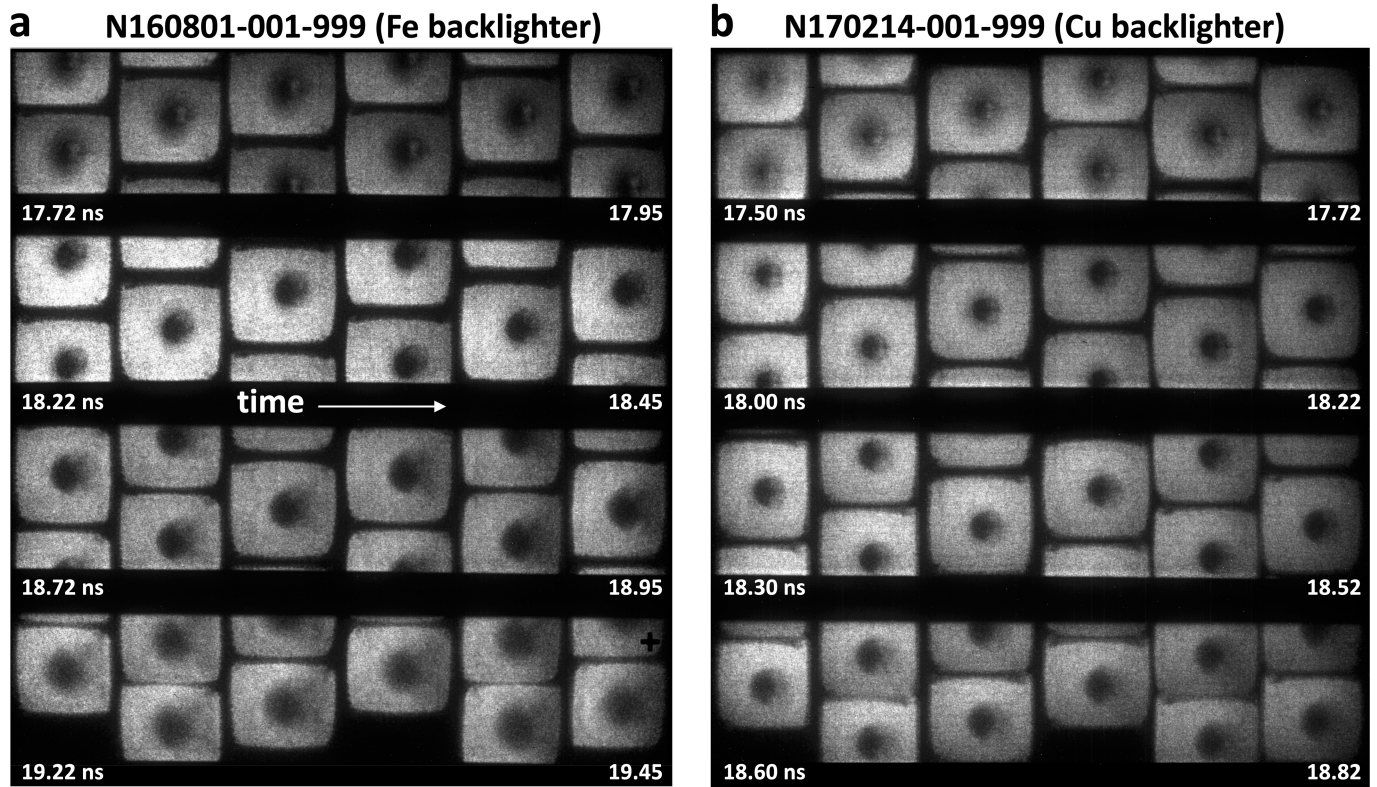


Extended Data Fig. 3 | X-ray Thomson scattering spectrum and fit for data set #4. The data (black) was recorded on experiment N180602-001-999 on the second spectrometer channel (strip 3) at 0.78 ns after peak emission, t_0 . The best fit (red), consisting of the free-free (blue), bound-free (green) and elastic scattering (purple) contributions, yields a temperature of $T = (160 \pm 20)$ eV, a free electron density of $n_e = (12 \pm 1.5) \times 10^{24} \text{ cm}^{-3}$ and an ion charge of $\bar{Z} = 3.3 \pm 0.1$ resulting in a mass density of $\rho = (55 \pm 8) \text{ g/cm}^3$ (see row #4 in Table 1).



Extended Data Fig. 4 | Radiation hydrodynamic simulations. Results of one-dimensional radiation-hydrodynamic simulations using the HYDRA code illustrating the implosion dynamics of the beryllium shell. These simulations are tuned to reproduce the observed timing of radiography experiment NI160801-001-999 (see also Extended Data Fig. 5a). (a) Simulation results for the evolution of the mass density and (b) a zoom-in for the behaviour close to stagnation. Panels (c) and (d) show radial profiles of mass density and temperature for different times near stagnation, respectively. The target geometry and the hohlraum radiation driving the implosion are shown in Fig. 1. The simulation predicts the highest core compression and peak x-ray emission at $t_0 = 17.9 \text{ ns}$. About 1 ns earlier, the main shock reaches the centre of the shell. As it is reflected and travels outwards, it sweeps up the in-falling shell material resulting in compression to mass densities of several 10s of g/cm^3 and a substantial temperature increase. Based on these simulations, and consistent

with the observation from the XRTS, the lower density tail of in-falling beryllium shell is minimized between 500 and 800 ps after peak x-ray emission. Note that this Be implosion design is very different from optimized high-performance implosions with deuterium-tritium (DT) fuel layers that aim for creating a burning plasma²⁴. Specifically, the Be shell is at a much higher adiabat (pressure over related Fermi pressure due to an elevated temperature) because (i) shocks are mistimed as shock timing was optimized for a corresponding experiment with a DT ice layer on the inside of the shell and (ii) the shell has no pre-heat shielding layer (usually made of Cu-doped Be near the inside surface). In addition, the implosion velocity is intentionally reduced by almost twofold to 200 km/s in order to reduce x-ray background signals for the XRTS measurements. All these facts contribute to an approximately tenfold reduced compression compared to what can be achieved in optimized layered implosions where the DT fuel reaches densities of $500 \text{ g}/\text{cm}^3$ and beyond.



Extended Data Fig. 5 | Raw data from radiography measurements near stagnation. Radiography data for two implosion experiments using the 2D-ConA platform³⁴ with (a) an Fe He- α area backlighter (6.7 keV) and (b) a Cu backlighter (8.4 keV). These measurements cover the probe times used for X-ray Thomson scattering measurements (18.2–18.7 ns). Peak x-ray emission (t_0) was observed at 17.88 ns and 17.91 ns for N160801 and N170214, respectively¹². The measurements use multi-pinhole ($d_{ph} = 20 \mu\text{m}$) imaging at 6 times magnification and capture about 40 images with 100 ps integration time on

4 multi-channel plate strips that are individually timed. Each strip covers a time period of 230 ps as indicated below the strips. The shell is initially held by a gold cone (cf. Fig. 1(g)), that is located on the right-hand side of the images, about 900 μm from the centre of the shell. The field of view of each of the frames is about $800 \times 800 \mu\text{m}^2$. Except for the backlighter material, the targets were identical within assembly tolerances and the experiments used the same laser drive request. The data demonstrate very good shot-to-shot repeatability in terms of implosion timing and shape of the imploded shell material.